Additive Manufacturing 46 (2021) 102180

Contents lists available at ScienceDirect

Additive Manufacturing

journal homepage: www.elsevier.com/locate/addma

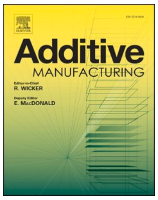

Additive manufacturing of high-performance vinyl ester resin via direct ink writing with UV-thermal dual curing

Ruowen Tu [a], Henry A. Sodano [a,b,c,*]

[a] Department of Aerospace Engineering, University of Michigan, Ann Arbor, MI 48109, USA
[b] Department of Materials Science and Engineering, University of Michigan, Ann Arbor, MI 48109, USA
[c] Department of Macromolecular Science and Engineering, University of Michigan, Ann Arbor, MI 48109, USA

ARTICLE INFO

Keywords:
Additive manufacturing
Direct ink writing
Vinyl ester
Unsaturated resin
UV-thermal dual curing

ABSTRACT

Vinyl ester (VE) resin is widely used as a thermosetting polymer for structural materials because of its high mechanical properties and excellent chemical resistance. Using additive manufacturing to produce high-performance VE structures with dimensional scalability and material efficiency has gained interest from both research and industry, however it is challenging due to the limitations of current techniques. In this work, a modified setup of direct ink writing (DIW) with ultraviolet (UV)-thermal dual curing is made compatible with commercially available VE resins thickened by 4 wt% fumed silica to fabricate three-dimensional structures with outstanding mechanical properties. The in-situ UV curing during DIW partially solidifies the resin to provide the structural shape, and subsequent thermal curing allows for a high degree of crosslinking. The printed and dual cured VE nanocomposites have a Young's modulus of 3.7 GPa and a tensile strength of approximately 80 MPa, which outperforms conventionally molded neat VE cured with methyl ethyl ketone peroxide (MEKP) by about 10% and also indistinguishable from the tensile properties of molded VE nanocomposites with the same composition. The fracture toughness of the printed and dual cured VE nanocomposites is also 16% higher than the molded neat VE with MEKP curing due to the superior interfacial bonding between DIW infill paths and the additional 4 wt% fumed silica for toughening, and similar to the molded VE nanocomposites with the same composition. Along with the outstanding mechanical properties, the scalability and resolution of the DIW technique with dual curing is demonstrated by printing a 100 mm long wrench and a microscale lattice, thus showing the potential of this technique in additive manufacturing of high-performance VE structures.

1. Introduction

Vinyl ester resin, or simply vinyl ester (VE), is a thermosetting polymer that possesses outstanding mechanical properties and excellent resistance to chemicals and moisture [1,2]. It is widely used in applications such as boats, infrastructure, and aircraft due to its superior mechanical strength, light weight, rapid cure, latency and low cost [3,4]. The traditional method for manufacturing three-dimensional (3D) structures comprised of thermosetting polymers is typically a molding process which involves high energy consumption and expensive molds. The recent advances in additive manufacturing, which are being increasingly applied in the automotive [5], aerospace engineering [6], biomaterials [7] and electronics industries [8], have led to extensive research interest and provide potential methods to manufacture thermosetting polymers in a scalable and cost-efficient way.

Among the various additive manufacturing techniques, vat photopolymerization, which uses a laser to photopolymerize a vat of resin layer by layer, is the most common method used to manufacture thermosetting polymers [9]. Typical resins used for vat photopolymerization include polyacrylate and epoxy monomers [9,10]. However, this technique has also been expanded to include elastomers and polymer ceramic composites [11,12]. In addition, researchers have applied vat photopolymerization to manufacture 3D VE structures by synthesizing VE resin with proper photo initiators. For example, Heller et al. investigated different VE-based monomers and synthesized suitable resin compositions for application in vat photopolymerization, which were used to build 3D biostructures [13]. The curing behavior of the novel VE-based resin for vat photopolymerization was further characterized by Hofstetter et al., who summarized the guidelines for using vat photopolymerization to fabricate VE structures and provided working

---

[*] Corresponding author at: Department of Aerospace Engineering, University of Michigan, Ann Arbor, MI 48109, USA.
E-mail address: hsodano@umich.edu (H.A. Sodano).

https://doi.org/10.1016/j.addma.2021.102180
Received 18 May 2021; Received in revised form 11 July 2021; Accepted 11 July 2021

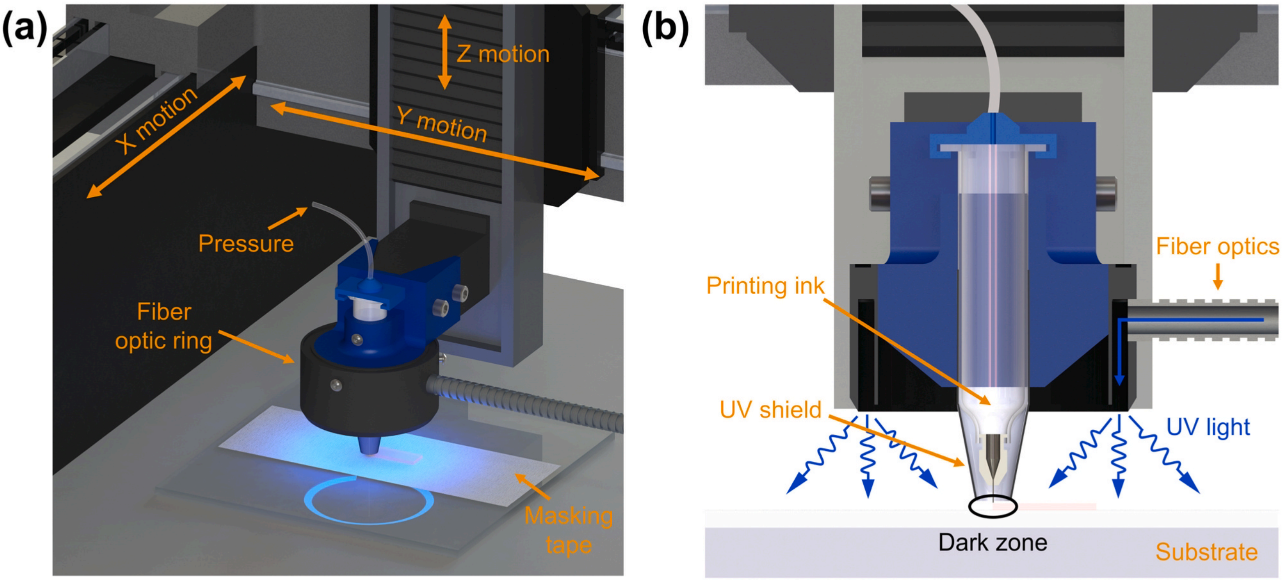

Fig. 1. (a) A modified UV-assisted DIW setup. (b) Cross-section view of the UV-assisted printing process (dark zone indicated with a black circle).

curves to correlate exposure, cure depth, double bond conversion and storage modulus [14]. Although these recent developments allowed for the fabrication of small-scale VE-based low toxicity biostructures using vat photopolymerization, manufacturing bulk VE structures to utilize its high mechanical properties as an engineering material has not yet been studied. In addition, vat photopolymerization requires a full vat of photocurable resin for operation which is not material-efficient and limits the development of new applicable resins. Direct ink writing (DIW), on the other hand, is an additive manufacturing technique that utilizes the rheological behavior (shear thinning) of the viscoelastic resin to form solid or semi-solid structures, with an optional post-curing process to allow for crosslinking [15]. Compared to vat photopolymerization, the amount of material required for DIW only depends on the volume of the final product, which ensures material efficiency. Moreover, DIW has been applied to fabricate 3D structures from different types of materials, such as thermosets [16], functional polymers [17], and polymer nanocomposites [18,19]. In spite of the wide range of applicable materials, DIW has strict requirements for the rheological behavior of the printing ink, which has limitations to process low viscosity resins like VE.

Recently, a modified DIW process with the addition of in-situ ultraviolet (UV) light curing that partially cures the printing ink for solidification during the DIW process was developed to expand the range of DIW applicable resins, which has been successfully demonstrated for the fabrication of architectures from epoxy [20,21], bismaleimide [22], carbon nanotubes/polymer nanocomposite [23], and even SiOC ceramic with the assistance of polysiloxane resin [24]. The in-situ UV curing allows for the use of low viscosity resins in the DIW process by partially curing the resin for solidification to maintain a structural shape, which is often then accompanied by a subsequent thermal curing step to induce a high degree of crosslinking, thus forming a UV-thermal dual curing process [25]. Such a technique has the potential of overcoming the challenges and limitations encountered when trying to additively manufacture high mechanical performance structures using low viscosity resins. Therefore, dual curing DIW can produce thermosetting structures capable of both high dimensional accuracy and excellent mechanical properties, which makes it a potential additive manufacturing technique for unsaturated thermosetting resins, such as VE.

This research is the first demonstration of using a modified setup of DIW with UV-thermal dual curing to fabricate high-performance VE 3D structures. The printing ink was based on commercially available VE resin thickened by fumed silica, which is a common rheological additive for resins [26], to obtain a balance between printability and final material stiffness. The dual curing process was characterized by performing Fourier-transform infrared spectroscopy (FTIR), differential scanning calorimetry (DSC), and dynamic mechanical analysis (DMA), while the mechanical properties of the final products were measured through tensile tests and single-edge-notch bending tests (SENB). Thermogravimetric analysis (TGA) was also performed on molded and printed samples to characterize the thermal stability of different VE resins. Finally, a 100 mm long wrench was fabricated to demonstrate the capability of producing bulk VE nanocomposite 3D structures, and a microscale lattice was printed to show its high printing resolution, thus proving this dual curing DIW method is a scalable technique to additively manufacture VE or other unsaturated resins.

2. Materials and methods

2.1. Printing ink preparation and rheological characterization

In order to study the printing ink rheology, 0–5 wt% fumed silica was added to the VE resin for resin thickening. For example, to prepare 10 g of printing ink with 4 wt% fumed silica, 9.255 g of VE resin (1110, Fibre Glast) was weighed in a vial, and then 0.4 g of fumed silica (CAB-O-SIL, CABOT) was added to the same vial along with 0.02 g polyvinylpyrrolidone (PVP) (average $M_W \sim 1300{,}000$, Sigma Aldrich), which acts as a surfactant for better dispersion. The printing ink was magnetically stirred for 30 min until a uniform suspension was obtained. Then 0.2 g of diphenyl(2,4,6-trimethylbenzoyl)phosphine oxide (TPO, Sigma Aldrich) was added as a photoinitiator, then the printing ink was stirred for another 30 min. Finally, 0.125 g of tert-Butyl peroxybenzoate (TBPB, 98%, Alfa Aesar) was added to the printing ink as a latent thermal radical initiator, which has a self-accelerating decomposition temperature (SADT) of 65.8 °C [32]. The printing ink was then stirred again for 30 min after which it could be used for printing or stored in a refrigerator (0 °C lifespan for approximately one week). Finally, the rheology behavior of the printing ink with different fumed silica content was characterized using a parallel-plate rheometer (Discovery HR20, TA Instruments), with an oscillation frequency sweep from 0.1 to 100 Hz, at 30 °C.

DIW Setup with Dual Curing.

First, the VE-based printing ink was loaded in a 10 mL syringe with a dispensing needle (32-gauge to 20-gauge, inner diameter ranges from

Table 1
The abbreviations of the different samples used in this work.

Abbreviation	Definition
UVE	Uncured neat VE
UVE-TBPB	Uncured VE with TBPB
UVE-MEKP	Uncured VE with MEKP
MVE-TBPB	Molded VE cured with TBPB
MVE-MEKP	Molded VE cured with MEKP
MVE/FS	Molded VE/fumed silica nanocomposite
PPVE/FS	Printed and photo cured VE/fumed silica
PDVE/FS	Printed and dual cured VE/fumed silica

0.10 mm to 0.61 mm), which was pneumatically controlled by a high precision dispenser (Ultimus V, Nordson EFD) as illustrated in Fig. 1a. A fiber optic ring light guide (Dolan-Jenner) was installed on a custom-designed holder, which connected the syringe and the fiber optics to a Cartesian gantry system (AGS1500, Aerotech). UV light (280–395 nm wavelength) was generated by a high-intensity light-curing system (BlueWave 200, Dymax) and guided through the fiber optic ring to deliver uniform UV radiation to the printing substrate. A glass plate covered with masking tape was used as the printing substrate for easy detachment of the sample from the substrate after the print was completed. After the UV-assisted DIW stage, a subsequential thermal curing process for 2 h in an oven at 100 °C was applied to samples for further crosslinking.

2.2. *Dual curing process characterization*

The abbreviations of the different samples used in this work are defined in Table 1 with their recipes listed in Table S1, and the following sections only use the abbreviations for simplicity. Among those, four different types of samples were used in the dual curing process characterization: MVE-MEKP using 1.25 wt% methyl ethyl ketone peroxide (MEKP, Fibre Glast), MVE-TBPB using 1.25 wt% TBPB, PPVE/FS (4 wt% fumed silica), and PDVE/FS (4 wt% fumed silica). Both types of molded neat VE samples were cured in an oven at 100 °C for 2 h, which was the same as the thermal curing stage for the PDVE/FS sample. Following the cure, multiple characterization methods were used to characterize the extent of cure and mechanical properties of the polymer. FTIR was performed using a Nicolet iS50 FTIR spectrometer with a Smart iTR Attenuated Total Reflectance (ATR) accessory on UVE and samples cured using the different curing processes. To measure the degree of cure a differential scanning calorimeter (Q2000, TA Instruments) was used to measure the heat of full curing reaction (ΔH_{full}) for uncured resins and the residual curing heat ($\Delta H_{residual}$) for the cured samples from different curing processes, with a temperature ramp from 25 °C to 250 °C at a rate of 5 °C min^{-1}. To measure the glass transition temperature (T_g) of the cured samples from the different curing processes, DMA (Q800, TA Instruments) in tension mode was applied to 30 mm × 7 mm × 1.5 mm rectangular samples with a 1 Hz sinusoidal strain of 0.05% amplitude and a temperature ramp from 25 °C to 200 °C at a rate of 5 °C min^{-1}. The glass transition temperature was then determined based on the storage modulus curve.

2.3. *Mechanical tests and thermogravimetric analysis*

Tensile tests were performed on VE samples according to ASTM D638, using an Instron 5982 universal testing system with a 100 kN load cell. The loading rate used in the tensile tests was 1.0 mm/min. Due to the high viscosity of the nanocomposite resin with 4 wt% fumed silica, the reference group MVE/FS samples were cured inside an autoclave with 30 psi (207 kPa) pressure at 100 °C for 2 h, to squeeze out the bubbles formed during the molding process. Considering the potential anisotropic material property of the PDVE/FS samples, samples printed with all 0°, all 90°, and 0°/90° alternating infill directions were tested and compared with molded samples. For all sample configurations, 6 specimens were tested to meet the statistics requirement for average and standard deviation calculations. Fracture toughness (critical-stress-intensity factor, K_{Ic}) measurements were conducted using a single-edge-notch bending (SENB) setup according to ASTM D5045-99, with sample dimensions shown in Fig. S1 and a loading rate of 10 mm/min. Surface morphology characterizations were performed using a field-emission scanning electron microscope (SEM, JEOL 2010F) and an atomic force microscope (AFM, Park Systems XE-70) in the non-contact mode. Thermogravimetric analysis (TGA) was applied to different cured samples using a thermal analyzer (Q600 SDT, TA Instruments), in the temperature range from 30 °C to 700 °C with a ramping rate of 15 °C min^{-1}.

3. Results and discussion

3.1. *Design of DIW with dual curing*

A novel UV-assisted DIW setup was designed in this research. A fiber optic ring light guide was installed on the Cartesian gantry system to provide uniform in-situ UV radiation, along with a syringe filled with printing ink placed at the center of the fiber optic ring. The syringe and dispensing needle were covered by a cone-shaped aluminum shield to form a dark zone around the needle tip (Fig. 1b) to avoid curing the resin

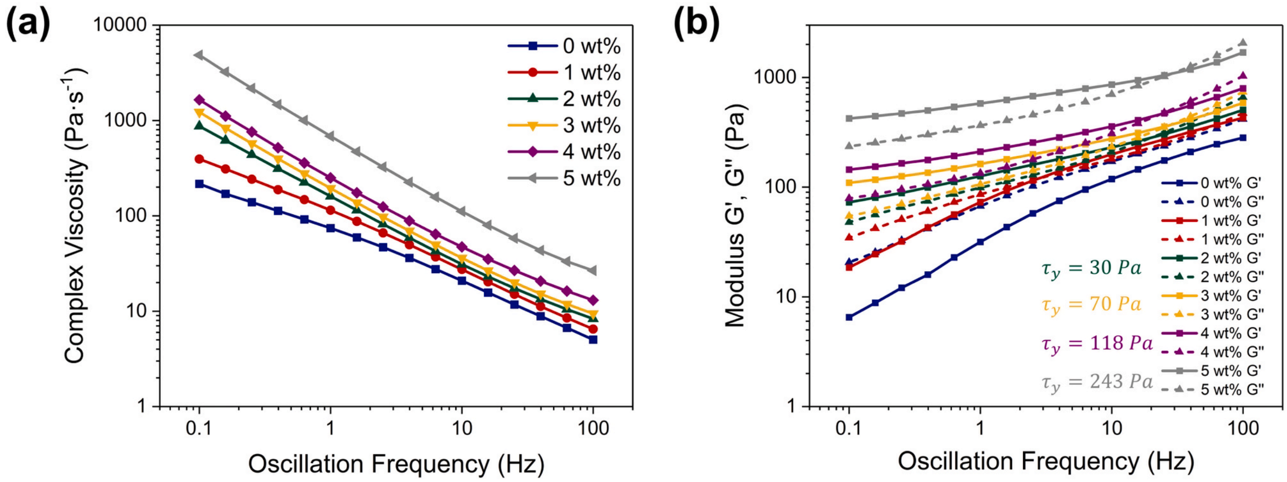

Fig. 2. (a) Complex viscosity of the printing ink with 0–5 wt% fumed silica under different oscillation frequencies. (b) Shear modulus G' and G'' of the printing ink with 0–5 wt% fumed silica under different oscillation frequencies.

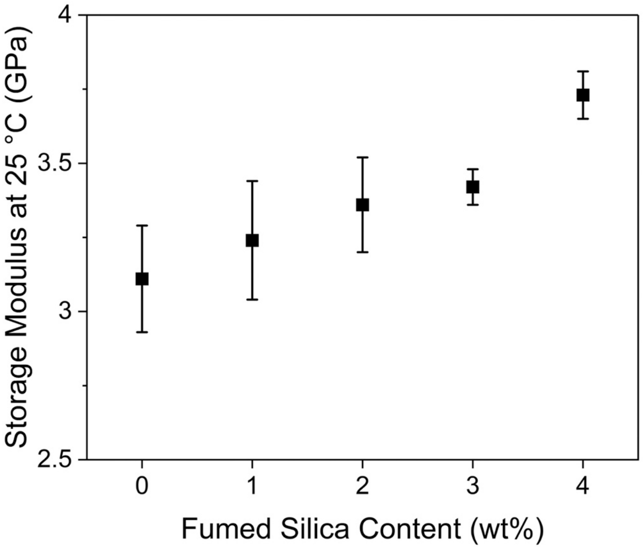

Fig. 3. Storage modulus of the printed and dual cured samples with 0–4 wt% fumed silica content at 25 °C.

at the tip. For comparison, existing UV-assisted DIW setups have either a UV light beam focused on the tip of the needle [22], which has the potential to clog the needle due to the resin curing at the tip, or a separate UV light which cures the resin only after each layer is completed [17,21], thus reducing the printing speed. The new setup proposed in this work has continuous and uniform UV radiation during the printing process and a UV shield to avoid tip clogging, thus providing both manufacturing efficiency and reliability (Fig. S2). Samples printed via this UV-assisted DIW were partially cured having a high stiffness and a precise 3D shape, and a subsequential thermal curing process for 2 h in an oven at 100 °C was applied to complete the material curing and obtain the full potential of the stiffness and strength.

3.2. Optimization of printing ink compositions

Neat VE resin has low viscosity at room temperature due to the presence of approximately 35–45 wt% styrene as a reactive diluent. This limits the DIW ability when using a needle size larger than 24-gauge (inner diameter 0.30 mm) since the resin is continuously dispensed out of the needle due to its own weight, without any applied pressure. Consequently, VE resins thickened by different weight fractions of fumed silica were tested to optimize the printing ink rheology and stiffness of the printed samples. To improve the dispersion of the fumed silica, 0.2 wt% PVP was also added as a surfactant to the VE resin. Fig. 2a shows the complex viscosity of the printing inks with 0–5 wt% fumed silica under different oscillation frequencies. From the figure, each of the printing inks exhibit a shear thinning behavior, where the complex viscosity decreases as the oscillation frequency increases. The addition of fumed silica increases the complex viscosity under all tested oscillation frequencies. Especially when increasing the fumed silica content from 4 wt% to 5 wt%, the complex viscosity rises drastically, which changes from 1648 Pa s^{-1} to 4840 Pa s^{-1} at 0.1 Hz low frequency. Although high viscosity ink with shear thinning behavior is desired for DIW, printing ink with 5 wt% or more fumed silica has extremely high viscosity at low frequency and requires large torque for stirring, which restricts the mixing performance of the magnetic stirring used to obtain a uniform suspension (supplementary video: *Printing ink viscosity with different fumed silica content.mov*). Shear storage modulus (G') and loss modulus (G'') are also important rheological properties of printing inks. For DIW, the printability requires G' exceeding G'' at low oscillation frequency, indicating a more elastic or solid-like rheological behavior [19,27,28]. According to Fig. 2b, printing inks with 2 wt% or more fumed silica exhibit higher G' than G'' at 0.1 Hz oscillation frequency, satisfying the printability requirement on shear modulus. In addition, the shear yield stress (τ_y), which is denoted by the shear stress where G' equals G'', is another property that quantifies the DIW printability [19]. The τ_y values of printing inks with 2 wt% or more fumed silica are listed in Fig. 2b, where higher fumed silica content results in higher τ_y which allows for the printed structure to deform elastically like a solid under a large shear stress without any permanent shape change. However, in this research, the modified UV-assisted DIW setup does not have such strict requirements on the printing ink rheological behavior due to the additional UV-triggered radical curing reaction outside the dark zone for solidification. On the other hand, the stiffness of the printed and dual cured samples, which is represented by the storage modulus at 25 °C, exhibits a gradual improvement as the fumed silica content increases (Fig. 3). Therefore, fumed silica not only acts as a resin thickener, but also provides additional mechanical reinforcement to the cured polymer. It should be noted that printing ink with 5 wt% fumed silica was not used for the DIW to produce dual cured samples, due to the difficulty in obtaining a uniform suspension. By considering the printing ink rheology, mixing difficulty and cured sample stiffness, ink with 4 wt% fumed silica was used to print samples for further mechanical characterization. In addition to the thickener and surfactant, 2 wt% TPO was added as a photoinitiator and 1.25 wt% TBPB was added as a latent thermal radical initiator for dual curing. It should be noted that the thermal radical initiator recommended by the manufacturer for VE molding process is MEKP, but it is not suitable for additive manufacturing because the curing reaction takes place at room temperature. Thus, latent TBPB was selected for DIW and all resultant mechanical characterization, while MVE-MEKP, MVE-TBPB, and MVE/FS nanocomposite with the same formula as the DIW printing ink act as reference groups. However, MVE/FS nanocomposite was only thermally cured, because the insufficient UV light penetration depth cannot provide a uniform degree of cure for the molded samples.

Supplementary material related to this article can be found online at doi:10.1016/j.addma.2021.102180.

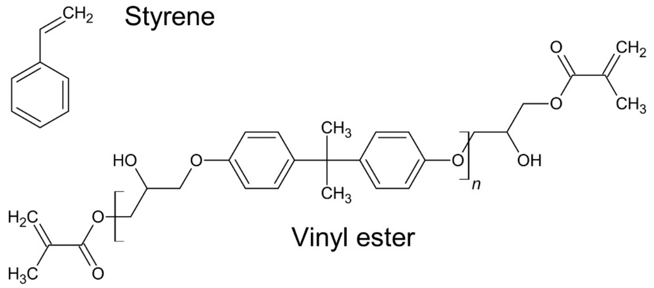

Fig. 4. Chemical structures of the VE resin.

3.3. Analysis of dual curing process

The chemical structures of the VE resin used in this research, which contains both VE and styrene (ST), are shown in Fig. 4.

The curing process of the printing ink was first characterized by performing FTIR on UVE, PPVE/FS, PDVE/FS, MVE-TBPB and MVE-MEKP samples. Fig. 5a shows the comparison of the four FTIR spectra in the wavenumber range of 650–1000 cm^{-1}. The curing of the VE resin, which consists of both ST and VE monomers, can be determined by monitoring the relative change in the amount of carbon-carbon double bonds (C=C) in both monomers during the curing reaction. The absorption peak at 910 cm^{-1} corresponds to the wagging of the CH_2 in the vinyl group of the ST monomers, while the absorption peak at 945 cm^{-1} is the bending of the C–H bond in the vinyl group of the VE monomers [29–31]. Since the change in absorbance intensity from FTIR can also be influenced by the sample thickness, the absorption peaks for the bending

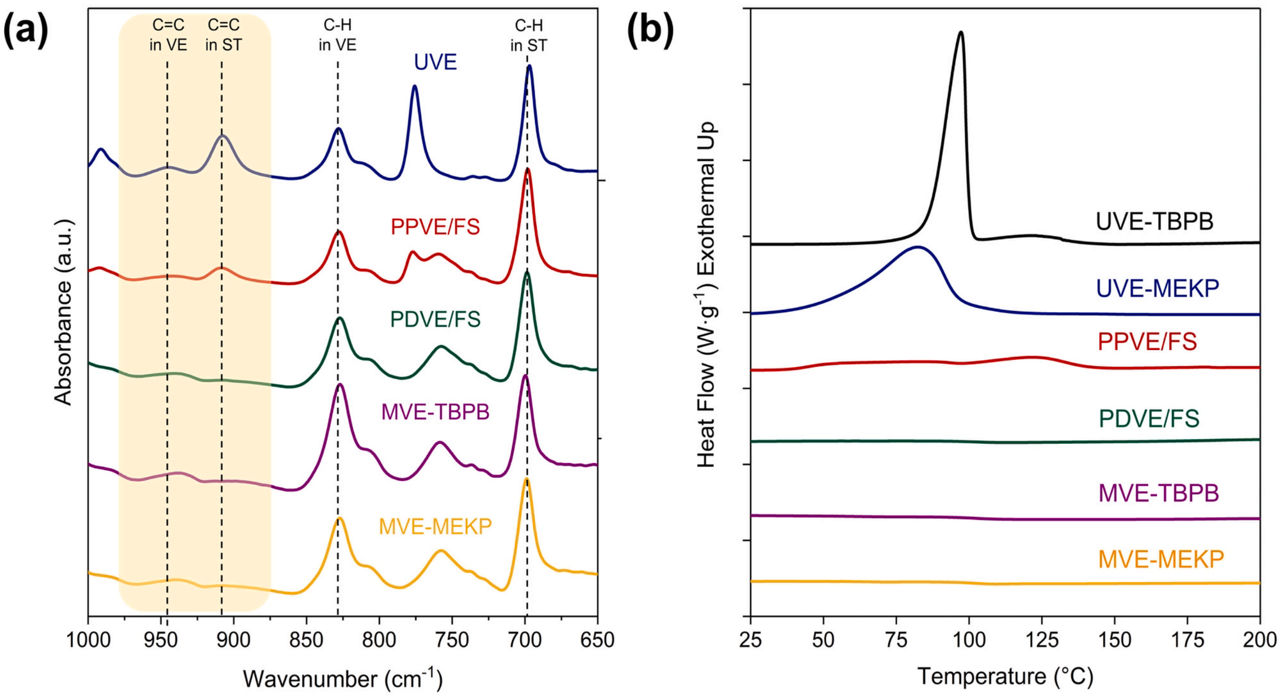

Fig. 5. (a) FTIR spectra of uncured, molded, and printed VE samples (curve deconvolution was performed on the cream-color boxed region). (b) DSC scans for uncured, molded, and printed VE samples from 25 °C to 200 °C.

Table 2
Fraction of conversion of both ST and VE monomers for different samples.

	α_{ST}	α_{VE}
PPVE/FS	66.8%	41.8%
PDVE/FS	95.3%	73.5%
MVE-TBPB	91.5%	72.1%
MVE-MEKP	92.3%	72.2%

of the aromatic C–H bond of the ST monomers (around 700 cm^{-1}) and the bending of the aromatic C–H bond of the VE monomers (around 830 cm^{-1}) can be used for the correction of absorbance intensity due to sample thickness [29–31]. According to a previous study by Brill and Palmese [29], Eqs. (1a) and (1b) can be used to calculate the fraction of converted ST and VE monomers:

$$\alpha_{ST} = 1 - \frac{A_{910,cured}}{A_{700,cured}} \times \frac{A_{700,uncured}}{A_{910,uncured}} \tag{1a}$$

$$\alpha_{VE} = 1 - \frac{A_{945,cured}}{A_{830,cured}} \times \frac{A_{830,uncured}}{A_{945,uncured}} \tag{1b}$$

where α_{ST} and α_{VE} are the fraction of conversion of the ST and VE monomers, respectively, and A is the peak absorbance intensity corresponding to the subscripted wavenumber (cm^{-1}) and sample type. It should be noted in the cured samples, the absorption peaks at 910 cm^{-1} and 945 cm^{-1} do not have sharp peak shapes due to the relatively low amount of C═C that exists in the cured samples. Therefore, curve deconvolution of the FTIR spectra using a Voigt profile was performed for the wavenumber range from 870 cm^{-1} to 970 cm^{-1} to obtain the peak absorbances at 910 cm^{-1} and 945 cm^{-1} while accounting for the baseline contribution. For reference, the deconvolution is shown in Fig. S3. Table 2 lists the results for PPVE/FS, PDVE/FS, MVE-TBPB and MVE-MEKP samples, which indicates that photo cured samples exhibit a lower fraction of conversion of both monomers relative to the dual cured or molded samples. Thus, the results confirm that the resin is not fully cured using only photo curing. This is mainly due to the limited penetration depth of UV light and the low exposure time for each layer during the DIW process. However, PDVE/FS samples show a fraction of conversion of both monomers at the same level as those of the reference MVE-TBPB and MVE-MEKP samples, with a ST conversion fractions more than 90%. The combination of these results indicate that the dual curing process can achieve a high degree of cure for the VE resin. It should be noted that the fraction of conversion of VE monomers is limited to about 70%, even for the manufacturer recommended MVE-MEKP samples, which is attributed to the relatively small size of the ST monomer which provides higher mobility, compared with the longer monomer chain of the VE monomer that limits diffusion for further polymerization.

Table 3
Heat of curing reaction and degree of cure calculated based on DSC data.

	ΔH_{full}	$\Delta H_{residual}$	Degree of cure
UVE-TBPB	337.3 J g^{-1}	/	/
UVE-MEKP	332.3 J g^{-1}	/	/
PPVE/FS	/	68.1 J g^{-1}	79.6%
PDVE/FS	/	3.3 J g^{-1}	99.0%
MVE-TBPB	/	0 J g^{-1}	100%
MVE-MEKP	/	0 J g^{-1}	100%

Fig. 5b shows the DSC scans for UVE-TBPB, UVE-MEKP, PPVE/FS, PDVE/FS, reference MVE-TBPB and MVE-MEKP samples, where the exothermal heat flow peaks indicate the heat generated during the curing reaction. While UVE-MEKP has a curing reaction that begins at room temperature, the curing reaction of UVE-TBPB begins at around 70 °C, which is above the self-accelerating decomposition temperature of TBPB, and it also has another shallow exothermal reaction peak from 100 °C to 140 °C caused by the rapid self-decomposition of the residual TBPB [32,33]. The PPVE/FS samples also exhibit a broad but shallow exothermal peak during the DSC scans, which indicates the existence of a residual curing reaction. The residual curing of the PPVE/FS samples starts at around 40 °C, which is lower than UVE-TBPB, due to the residual photo-initiated free radicals in the PPVE/FS samples having higher mobility at elevated temperatures for further polymerization. Similarly, the shallow exothermal reaction peak in the printed and photo cured sample from 100 °C to 140 °C is the rapid self-decomposition of

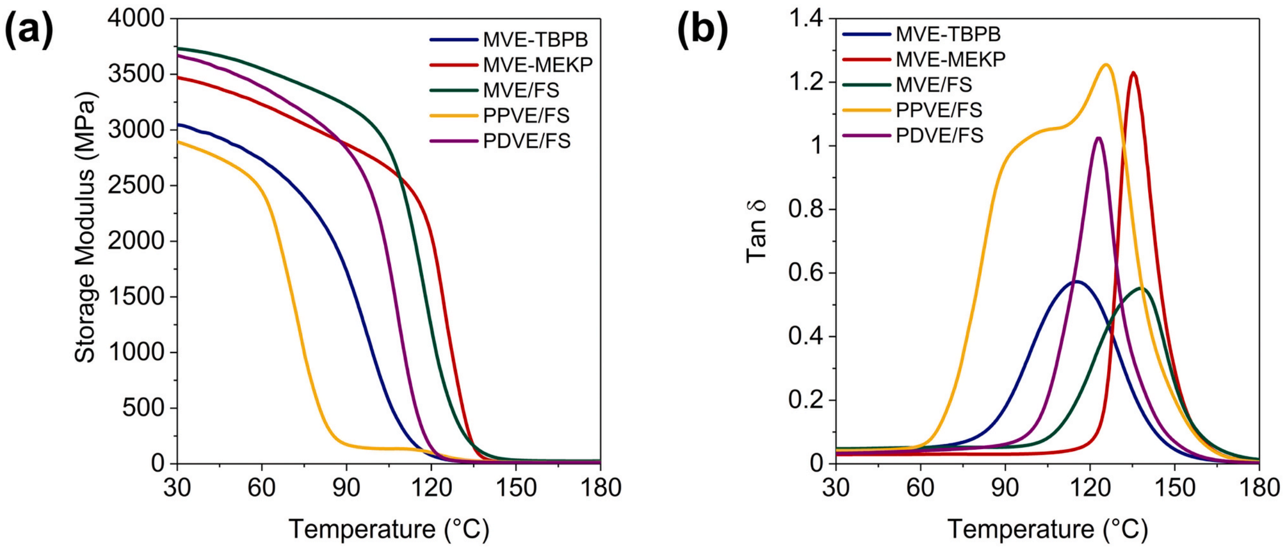

Fig. 6. (a) Storage modulus of the five types of samples in the temperature range from 30 °C to 180 °C. (b) Tan δ of the five types of samples in the temperature range from 30 °C to 180 °C.

the residual TBPB. On the other hand, the PDVE/FS samples show no clear exothermal peak during DSC scans like the reference MVE-TBPB or MVE-MEKP, suggesting the samples are fully cured. By integrating the heat flow peak over the curing reaction duration, the heat of the full curing reaction (ΔH_{full}) for uncured resin and the residual curing heat ($\Delta H_{residual}$) for cured samples and the degree of cure is calculated following Eq. (2) and listed in Table 3.

$$Degree \quad of \quad cure = 1 - \frac{\Delta H_{residual}}{\Delta H_{full}} \tag{2}$$

It should be noted that the heat of the full curing reaction measured for the UVE-TBPB or UVE-MEKP is within a 2% difference regardless of the initiator; thus, their average (334.8 J g^{-1}) is used for the degree of cure calculation. While the PPVE/FS samples only have 79.6% degree of cure, the PDVE/FS samples have close to 100% degree of cure like the reference MVE-TBPB and MVE-MEKP, which is consistent with the results from FTIR. Both FTIR and DSC characterization results show that samples produced by DIW with dual curing produce fully cured samples, which is comparable to the MVE-MEKP samples according to the manufacturer recommendations.

DMA was then applied to PPVE/FS, PDVE/FS, MVE-TBPB, MVE-MEKP and MVE/FS samples to determine the viscoelastic properties. For reference, Fig. S4 shows the different colors of the cured samples where the PPVE/FS sample initially has a creamy pink color which changes to a green-amber color after the thermal curing with TBPB as the radical initiator. The storage modulus results in Fig. 6a shows that with only the first step photo curing, the partially cured PPVE/FS sample has 95% storage modulus at room temperature relative to the MVE-TBPB sample, 84% relative to the MVE-MEKP sample, or 79% relative to the MVE/FS sample. However, the PPVE/FS sample has a transition from a glassy state to a rubbery state at a much lower temperature, which starts at around 60 °C, compared to all molded samples. The rubbery state of the PPVE/FS sample has two different stages (Fig. 6a): stage 1 from 80 °C to 115 °C, which is distinct from the molded samples (also shows a tan δ shoulder in Fig. 6b); and stage 2 above 130 °C, which is similar to all three molded samples. The distinct stage 1 can be explained by the further curing of the VE due to the higher mobility of the residual photo-initiated free radicals during the DMA temperature ramp. In contrast, the PDVE/FS sample shows a 21% and 7% higher storage modulus at room temperature relative to the MVE-TBPB and MVE-MEKP samples, respectively, and only 2% lower than the storage modulus of MVE/FS sample. Furthermore, the transition from glassy to rubbery state of the PDVE/FS sample happens at a higher temperature relative to the PPVE/FS sample. The glass transition temperatures (T_g) for the five types of samples defined by the storage modulus curves are listed in Table 4. The PDVE/FS sample (using TBPB as the thermal radical initiator) has a 10 °C increase in T_g compared to the MVE-TBPB sample, which is explained by the contribution from the fumed silica and surfactant PVP that restrain the polymer chain movement at high temperatures. However, the T_g of the PDVE/FS sample is still lower than MVE/FS and MVE-MEKP, possibly caused by the different initiator chemistry or the photo curing process that reduces the overall crosslinking density.

Table 4
Glass transition temperatures (T_g) of five types of samples.

Sample Type	T_g
MVE-TBPB	97.7 °C
MVE-MEKP	126.9 °C
MVE/FS	117.4 °C
PPVE/FS	73.6 °C
PDVE/FS	108.2 °C

3.4. *Mechanical properties of the PDVE/FS nanocomposites*

After the dual curing process for DIW of VE resin was characterized, tensile tests and SENB tests were performed to measure the mechanical properties of the PDVE/FS samples. To note that, the reference groups for mechanical testing are MVE-TBPB, MVE-MEKP, and MVE/FS, to compare the mechanical properties of PDVE/FS with commercially available neat VE and the molded VE/fumed silica nanocomposites with the same formula as the printing ink. For the tensile tests, since additively manufactured parts often have anisotropic mechanical properties due to the directionality of infill paths [34,35], samples printed with all 0° (parallel to the loading axis), all 90° (perpendicular to the loading axis), and 0°/90° alternating infill directions were tested and compared with molded samples. Fig. 7a shows that PDVE/FS has a Young's modulus 20% higher than MVE-TBPB and 10% higher than MVE-MEKP, regardless of the infill direction. One-way ANOVA analysis ($\alpha = 0.05$) also proves that the Young's modulus of the PDVE/FS samples does not depend on the infill direction, and has no significant difference compared to MVE/FS samples. The tensile strength of the 0° samples is the highest among all infill directions at 20% and 8% higher than the

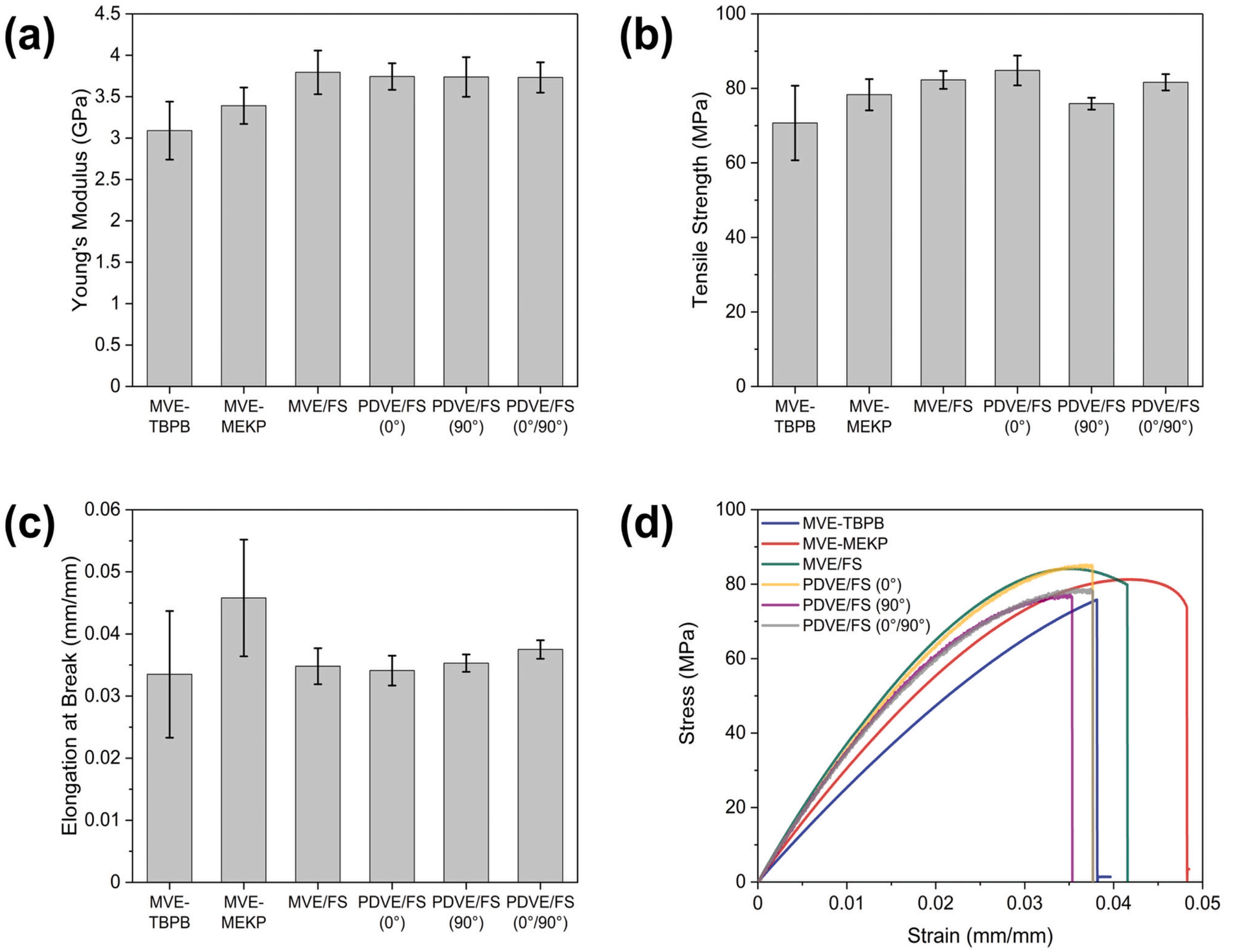

Fig. 7. Tensile test results for MVE-TBPB, MVE-MEKP, MVE/FS, and PDVE/FS with different infill directions: (a) Young's modulus; (b) tensile strength; (c) elongation at break; (d) typical stress-strain curves.

MVE-TBPB and MVE-MEKP samples, respectively, while the 90° samples only have a 3% lower tensile strength compared to the MVE-MEKP samples, still higher than the MVE-TBPB samples (Fig. 7b). Compared to MVE/FS, while the 90° PDVE/FS has 8% lower tensile strength, both the 0° and 0°/90° alternating samples have similar tensile strength as MVE/FS. Although the tensile strength of PDVE/FS does depend on the infill direction according to the one-way ANOVA analysis, the cause of this slight anisotropy is not the low adhesion or weak bonding between adjacent infill paths, but an increase in the probability of small bubbles forming between infill paths during printing. Since the specimens used for tensile testing are long and narrow, the 90° infill direction results in a higher number of interfaces between infill paths, thus a higher probability of forming small bubbles relative to the 0° infill direction. These small bubbles are defects and are form the location where failure is initiated. The difference in tensile strength among all infill directions is within 10%, which is less significant than the anisotropy due to weak interfacial bonding [36]. The elongation at break of PDVE/FS does not depend on the infill direction based on one-way ANOVA analysis ($\alpha = 0.05$), and is similar to the elongation at break of MVE-TBPB and MVE/FS, but lower than that of MVE-MEKP (Fig. 7c). Fig. 7d shows typical stress-strain curves for the different types of samples, where MEKP cured VE exhibits higher elongation at break than TBPB cured VE (both molded and printed), due to the different curing kinetics of the two radical initiators that cause the variation in number of interior defects formed during the curing process.

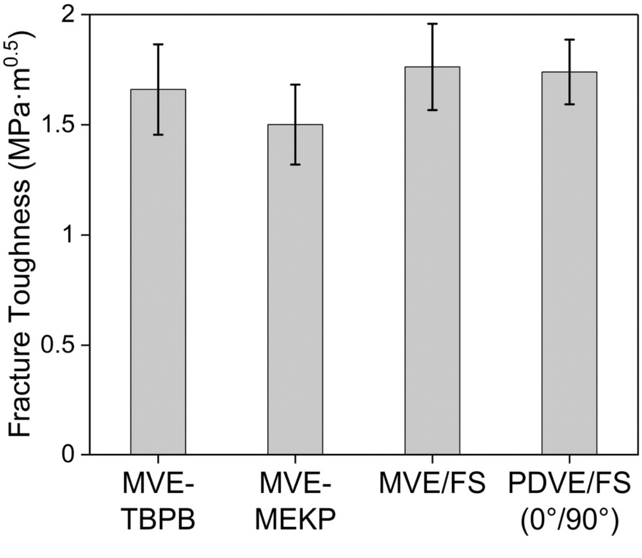

Fig. 8. Fracture toughness (critical-stress-intensity factor) of the MVE-TBPB, MVE-MEKP, MVE/FS, and PDVE/FS (0°/90°) samples.

The fracture toughness (critical-stress-intensity factor, K_{Ic}) of the

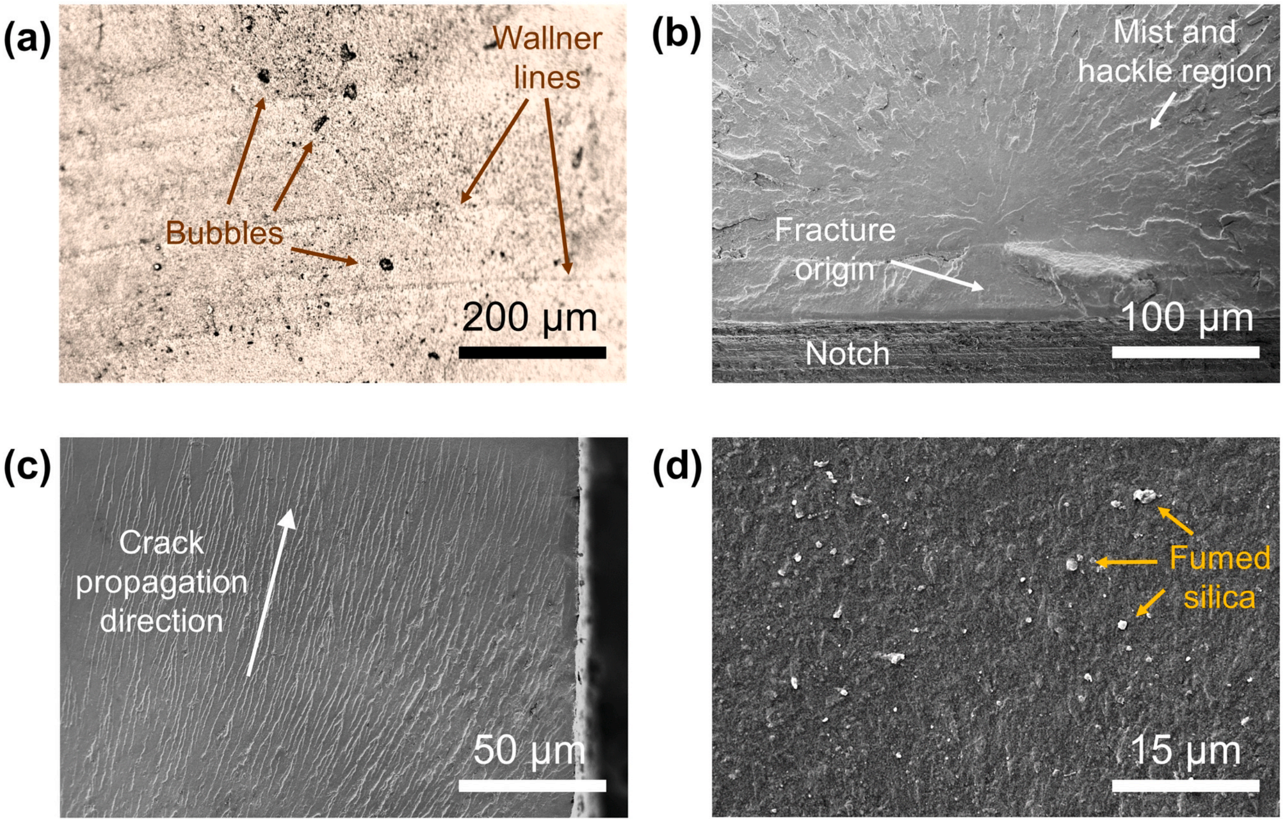

Fig. 9. (a) Optical microscope image of a fracture surface, where dark spots are few bubbles formed during printing. (b) SEM image of the fracture surface near the notch. (c) SEM image of the fracture surface remote from the fracture origin. (d) High-magnification SEM image of the rough fracture surface and well-dispersed fumed silica.

PDVE/FS was measured based on SENB tests and compared to MVE-TBPB, MVE-MEKP, and MVE/FS, which is shown in Fig. 8. It should be noted that since tensile test results have confirmed that the mechanical properties of the PDVE/FS show no significant dependence (within 10% difference) on the infill directions, 0°/90° alternating infill samples, which are the most practically used in the additive manufacturing industry, were used for SENB tests. The measured fracture toughness of the PDVE/FS samples is 5% higher than the MVE-TBPB samples, and 16% higher than the MVE-MEKP samples (Fig. 8). Based on the one-way ANOVA analysis ($\alpha = 0.05$), the fracture toughness of the PDVE/FS samples has negligible difference relative to the MVE/FS samples. The high fracture toughness of the PDVE/FS is attributed to the toughening effect of the 4 wt% fumed silica and improved interfacial strength between the fumed silica and VE due to the 0.2 wt% high molecular weight PVP. It should be noted that all measured fracture toughness values of the different VE samples are slightly higher than the fracture toughness of neat VE reported in other works [37–39] due to the relatively low curing temperature and no post-curing process used in this work which results in a lower degree of crosslinking and brittleness. Fig. 9a shows an optical microscope image of the fracture surface of a representative PDVE/FS sample with some faint concentric Wallner lines, where the dark spots are few bubbles formed during DIW printing as mentioned previously. However, there is no clear boundary between infill paths that can be observed at the fracture surface, which confirms that sufficient interfacial bonding occurs between adjacent paths during printing. Fig. 9b and c are SEM images of the PDVE/FS fracture surface, where a fracture origin surrounded with radiating mist and hackle regions can be clearly identified, and the crack propagation direction can be determined by the hackle marks remote from the fracture origin. Fig. 9d is a high-magnification SEM image of the fracture surface, where abundant well-dispersed fumed silica particles are present on the rough surface to hinder the propagation of cracks, thus improving the fracture toughness. A more detailed fractography analysis of the PDVE/FS compared to the reference MVE-TBPB, MVE-MEKP and MVE/FS is included in the Supporting Information document.

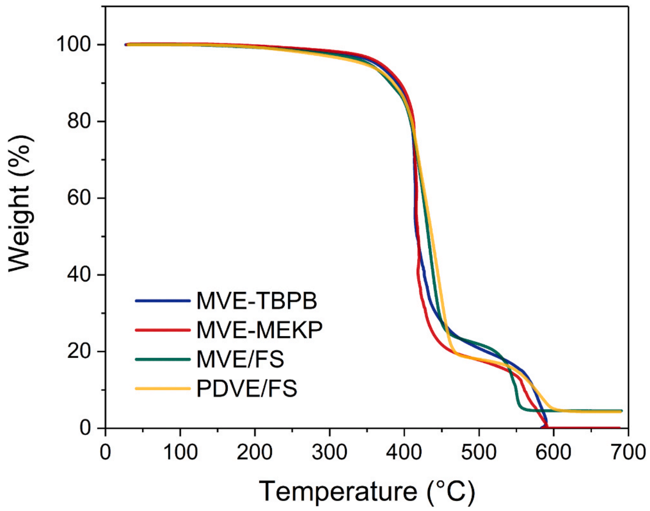

Fig. 10. TGA of the molded and printed samples.

Both tensile and SENB test results show that the PDVE/FS has comparable or even higher mechanical properties relative to the molded neat VE resins, and negligible difference compared to the molded nanocomposites with the same composition. Compared to other additive manufacturing methods for polymers, such as material extrusion and original DIW, where the extruded material solidifies immediately before

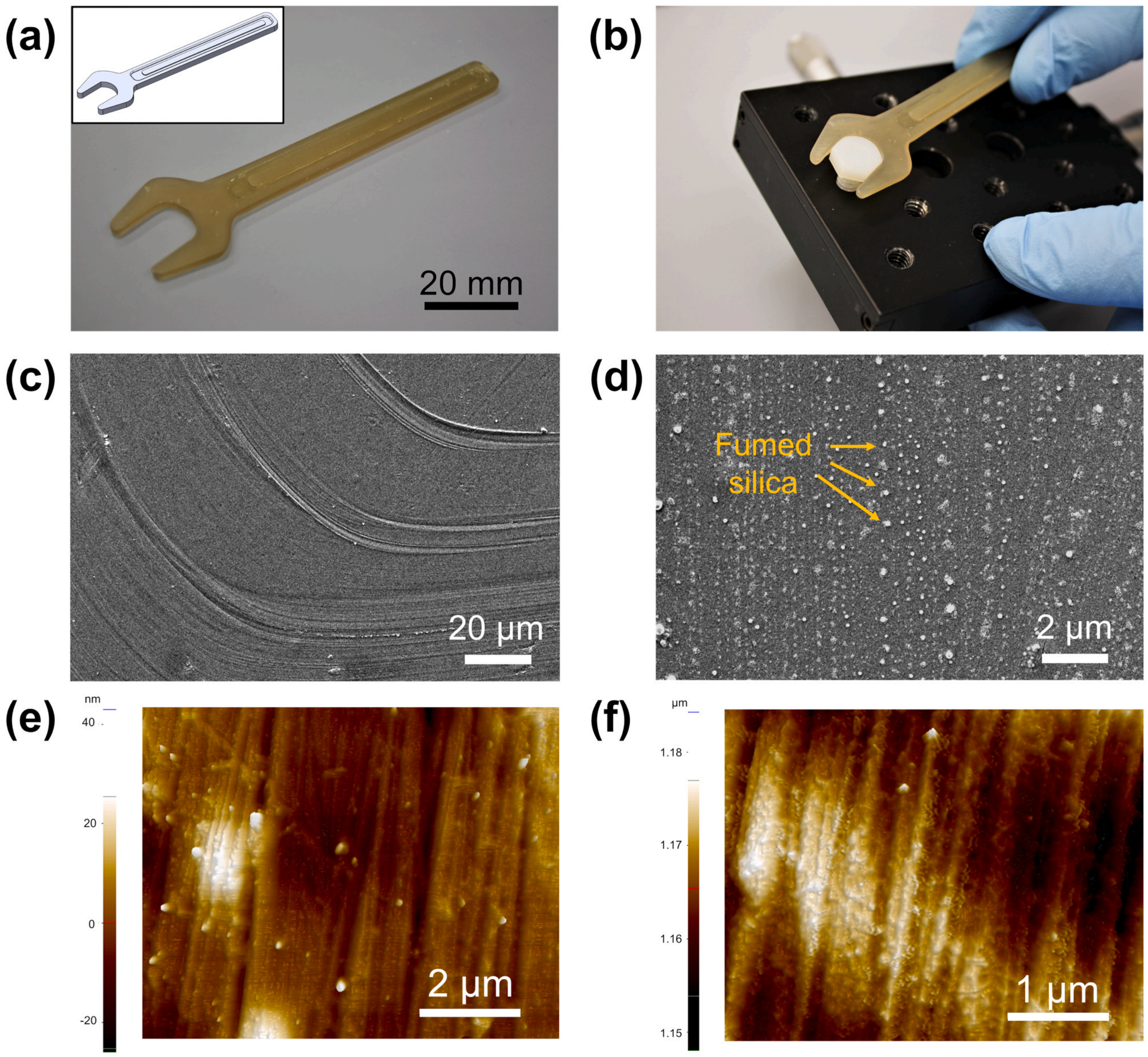

Fig. 11. (a) A PDVE/FS wrench. (b) The printed wrench was used to tighten a US 1/4–20 hex bolt. (c) & (d) SEM images of the wrench surface. (e) & (f) AFM images of the wrench surface.

joining the adjacent path for a sufficient interfacial bonding, the UV-assisted DIW employed in this work uses paste-like semi-liquid ink that can slowly flow around and fill gaps within the dark zone (Fig. 1b), which is then subsequently cured by the UV light to form solid shapes, thus ensuring good interfacial bonding. This alteration to the DIW process, along with the strengthening effect from the 4 wt% fumed silica, provide PDVE/FS with outstanding mechanical properties, while the additive manufacturing nature also allows for scalability and design freedom.

3.5. *Thermal stability of the PDVE/FS nanocomposites*

Fig. 10 shows the thermal decomposition of MVE-TBPB, MVE-MEKP, MVE/FS and PDVE/FS in air up to 700 °C, where MVE-TBPB and MVE-MEKP have final weight percentage of 0% while MVE/FS and PDVE/FS have around 4% silica left. Decomposition temperature (T_d), defined by the temperature for a material to have at least 5% weight loss, can be used to determine the thermal stability of the molded and printed VE samples. PDVE/FS and MVE/FS have a T_d of 346 °C and 352 °C, respectively, both about 5% lower than the T_d of MVE-TBPB or MVE-MEKP. This result indicates that the VE/fumed silica nanocomposites have slightly lower thermal stability compared to the neat VE resins. However, with the same temperature ramp rate (15 °C min^{-1}) used in TGA, the VE/fumed silica nanocomposites show a slower decomposition rate than neat VE resins in the temperature range from 400 °C to 450 °C.

3.6. *Printed 3D structures*

As an additive manufacturing technique, DIW with UV-thermal dual curing is capable of fabricating 3D structures with complex geometries. Fig. 11a shows a PDVE/FS wrench with dimensions of approximately 100 mm in length and 3.5 mm in thickness, compared with the designed shape shown on the top left to show the capability of this technique to additively manufacture 3D structures with high dimensional accuracy. The printed wrench is sufficiently strong and stiff to be practically used for tightening a US 1/4-20 hex bolt (Fig. 11b). The surface morphology of the printed wrench was characterized using both SEM and AFM imaging on the curved groove region of the wrench handle (Fig. S9, S10

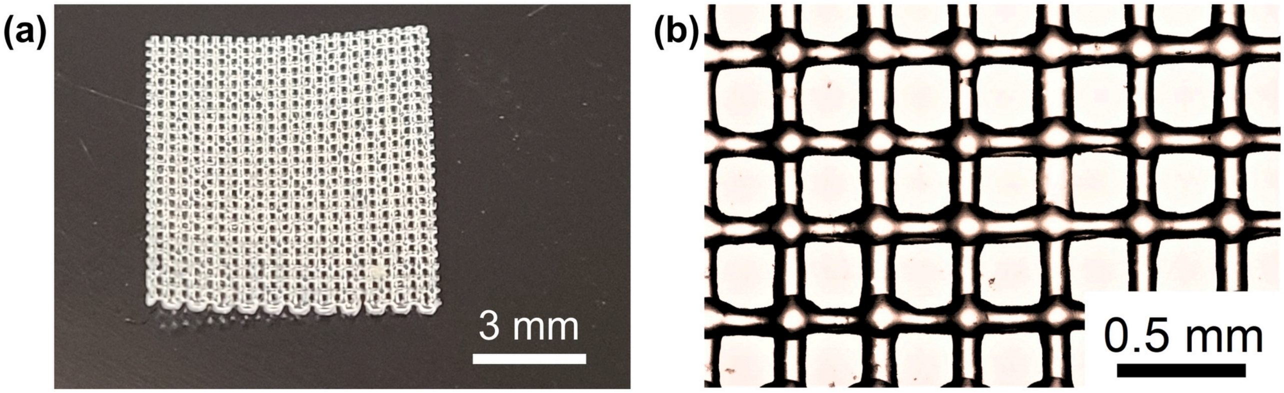

Fig. 12. (a) A printed microscale lattice to show high printing resolution. (b) Optical microscope image of the printed microscale lattice.

Table 5
Actual dimensions and errors of molded and printed samples.

	MVE-TBPB	MVE-MEKP	MVE/FS	PDVE/FS (0°/90°)
Average (mm)	6.94	6.93	6.88	6.91
Standard Deviation (mm)	0.06	0.05	0.09	0.05
Relative Error to the Designed Value	-2.2%	-2.3%	-3.1%	-2.7%

and S11). Fig. 11c is an SEM image that shows the overlapping of two adjacent curved infill paths, which causes some visibly bumpy surface. Fig. 11d is another zoomed-in SEM image showing some fumed silica-rich (white dots) areas on the wrench surface. The more detailed surface morphology is illustrated in Fig. 11e and f via AFM imaging, where the localized surface roughness is caused by the agglomerated fumed silica (bright spots). According to AFM, the root mean square roughness of the printed wrench surface ranges from 3 to 24 nm, while the average roughness ranges from 2 to 18 nm. Therefore, the printed surfaces are generally smooth in a large scale while having some bumpy regions around the infill path interfaces, and the surface roughness is also caused by the agglomerated fumed silica.

In addition to the capability of printing high strength engineering structures, the technique developed in this work also allows for high resolution printing by using a micro precision nozzle (32-gauge, inner diameter 100 μm). Fig. 12a shows a printed 3D microscale lattice with 240 μm thickness (20 μm thick each layer), where the printed line width is approximately 100–120 μm measured using optical microscope imaging (Fig. 12b). Therefore, DIW with the UV-thermal dual curing provides a scalable approach to additively manufacture VE nanocomposites with excellent mechanical properties and high resolution.

3.7. Dimensional accuracy and printing speed

Dimensional accuracy is another important criterion to evaluate the performance of an additive manufacturing method. Table 5 shows the measured width and errors of MVE-TBPB, MVE-MEKP, MVE/FS and PDVE/FS (0°/90°) bar-shape samples with a designed width of 7.1 mm, where all of them exhibit a 2–3% lower width relative to the design value due to inevitable cure shrinkage. However, by using a one-way ANOVA analysis ($\alpha = 0.05$), the resulting p-value of the four groups of data is 0.48, which means no significant difference can be found among these four types of samples. The statistic results show that the printed VE has a similar dimensional accuracy compared to molded VE, while all VE samples are subject to cure shrinkage.

In addition to the dimensional scalability that has been demonstrated in the previous section, the scalability of an additive manufacturing method is also related to the printing speed. For this DIW method with dual curing, the printing speed depends on the needle size and the moving speed but is limited by the UV curing rate of the resin. The layer thickness is limited by the penetration depth of the UV light, according to which we found 0.1 mm is the maximum layer thickness for adequate UV curing. Table S2 shows a summary of the printing parameters that were adopted in this work. When printing the 100 mm long wrench sample, it took approximately 6 h using a 26-gauge needle and 0.05 mm layer thickness to ensure printing resolution and quality, but it could be reduced to 1.2 h if we used a 20-gauge needle and 0.1 mm layer thickness. For even larger dimension prints, since the area of each layer is bigger, the printing speed can be increased while still keeping an adequate UV irradiation time for each layer to cure. We tested a printing parameter set of 20-gauge needle, 0.5 mm infill path width, 0.1 mm layer thickness, 28 mm/s moving speed and 1.8 psi (12.4 kPa) pressure to print a 70 mm × 70 mm × 1 mm square, and it only took about 1 h compared to about 11 h if we used the same setting (26-gauge) for the wrench sample. Therefore, using a larger needle and a faster moving speed can potentially increase the printing efficiency of this technique, but it is limited by the UV irradiation time for each layer to cure. For future work, a customized slicing software can be developed which allows to calculate the optimal moving speed for each layer based on the infill area, geometry and UV curing rate.

4. Conclusions

A modified setup of DIW with UV-thermal dual curing provides a scalable and material-efficient way of fabricating 3D VE nanocomposite structures from commercially available VE resins thickened by fumed silica. A fumed silica content of 4 wt% is chosen as the optimal printing ink composition by considering the printing ink rheological behavior, mixing difficulty and the final product stiffness. The VE nanocomposites processed using this technique has a comparable degree of cure to conventionally molded VE, but has a slightly lower glass transition temperature at 108.2 °C. The printed and dual cured VE nanocomposites exhibit outstanding mechanical properties and low anisotropy, as it has a Young's modulus of 3.7 GPa and tensile strength about 80 MPa, which are both higher than the properties of molded neat VE and indistinguishable from the molded VE nanocomposites. The sufficient interfacial bonding between infill paths and additional 4 wt% silica also make the printed and dual cured VE nanocomposites 16% tougher than the molded neat VE with MEKP curing, and have no significant difference compared to the molded VE nanocomposites. TGA shows that printed VE nanocomposites have slightly weaker thermal stability than the neat VE resins, quantified by a 5% lower T_d. In addition, a 100 mm long wrench and a microscale lattice are printed to demonstrate the dimensional scalability and high resolution of this technique to produce 3D VE nanocomposite structures. Therefore, DIW with UV-thermal dual curing is shown to be an effective additive manufacturing technique for high-performance VE resins, which also has the potential of being applied to other unsaturated resins.

CRediT authorship contribution statement

Ruowen Tu: Conceptualization, Visualization, Investigation, Formal analysis, Writing - Original Draft. **Henry A. Sodano:** Conceptualization, Supervision, Writing - Review & Editing.

Declaration of Competing Interest

The authors declare the following financial interests/personal relationships which may be considered as potential competing interests: Henry Sodano reports financial support was provided by National Science Foundation. Ruowen Tu reports financial support was provided by National Science Foundation.

Acknowledgments

The authors gratefully acknowledge support for this work from the National Science Foundation under Grant # EFRI-1935216 and the Air Force Office of Scientific Research under Contract # FA9550-16-1-0087.

Appendix A. Supporting information

Supplementary data associated with this article can be found in the online version at doi:10.1016/j.addma.2021.102180.

References

[1] Z. Guo, X. Liang, T. Pereira, R. Scaffaro, H. Thomas Hahn, CuO nanoparticle filled vinyl-ester resin nanocomposites: fabrication, characterization and property analysis, Compos. Sci. Technol. 67 (2007) 2036–2044, https://doi.org/10.1016/j.compscitech.2006.11.017.

[2] M.B. Launikitis, Vinyl Ester Resins, in: G. Lubin (Ed.), Handbook of Composites, Springer, US, Boston, MA, 1982, pp. 38–49, https://doi.org/10.1007/978-1-4615-7139-1_3.

[3] B.K. Kandola, J.R. Ebdon, C. Zhou, Development of vinyl ester resins with improved flame retardant properties for structural marine applications, React. Funct. Polym. 129 (2018) 111–122, https://doi.org/10.1016/j.reactfunctpolym.2017.08.006.

[4] F. McBagonluri, K. Garcia, M. Hayes, K.N.E. Verghese, J.J. Lesko, Characterization of fatigue and combined environment on durability performance of glass/vinyl ester composite for infrastructure applications, Int. J. Fatigue 22 (2000) 53–64, https://doi.org/10.1016/S0142-1123(99)00100-0.

[5] D. Böckin, A.-M. Tillman, Environmental assessment of additive manufacturing in the automotive industry, J. Clean. Prod. 226 (2019) 977–987, https://doi.org/10.1016/j.jclepro.2019.04.086.

[6] A. Uriondo, M. Esperon-Miguez, S. Perinpanayagam, The present and future of additive manufacturing in the aerospace sector: a review of important aspects, Proc. Inst. Mech. Eng. Part G J. Aerosp. Eng. 229 (2015) 2132–2147, https://doi.org/10.1177/0954410014568797.

[7] F. Liravi, E. Toyserkani, A hybrid additive manufacturing method for the fabrication of silicone bio-structures: 3D printing optimization and surface characterization, Mater. Des. 138 (2018) 46–61, https://doi.org/10.1016/j.matdes.2017.10.051.

[8] N. Saengchairat, T. Tran, C.-K. Chua, A review: additive manufacturing for active electronic components, Virtual Phys. Prototyp. 12 (2017) 31–46, https://doi.org/10.1080/17452759.2016.1253181.

[9] F.P.W. Melchels, J. Feijen, D.W. Grijpma, A review on stereolithography and its applications in biomedical engineering, Biomaterials 31 (2010) 6121–6130, https://doi.org/10.1016/j.biomaterials.2010.04.050.

[10] P. Jacobs, Stereolithography 1993: epoxy resins, improved accuracy, and investment casting, in: Coupling Technology to National Need, International Society for Optics and Photonics, 1994: pp. 41–52. ⟨https://doi.org/10.1117/12.170612⟩.

[11] N. Bhattacharjee, C. Parra-Cabrera, Y.T. Kim, A.P. Kuo, A. Folch, Desktop-stereolithography 3D-printing of a poly(dimethylsiloxane)-based material with Sylgard-184 properties, Adv. Mater. (Deerfield Beach Fla.) 30 (2018), 1800001, https://doi.org/10.1002/adma.201800001.

[12] F. Doreau, C. Chaput, T. Chartier, Stereolithography for manufacturing ceramic parts, Adv. Eng. Mater. 2 (2000) 493–496, https://doi.org/10.1002/1527-2648(200008)2:8<493::AID-ADEM493>3.0.CO;2-C.

[13] C. Heller, M. Schwentenwein, G. Russmueller, F. Varga, J. Stampfl, R. Liska, Vinyl esters: low cytotoxicity monomers for the fabrication of biocompatible 3D scaffolds by lithography based additive manufacturing, J. Polym. Sci. Part A Polym. Chem. 47 (2009) 6941–6954, https://doi.org/10.1002/pola.23734.

[14] C. Hofstetter, S. Orman, S. Baudis, J. Stampfl, Combining cure depth and cure degree, a new way to fully characterize novel photopolymers, Addit. Manuf. 24 (2018) 166–172, https://doi.org/10.1016/j.addma.2018.09.025.

[15] J.A. Lewis, Direct ink writing of 3D functional materials, Adv. Funct. Mater. 16 (2006) 2193–2204, https://doi.org/10.1002/adfm.200600434.

[16] K.B. Manning, N. Wyatt, L. Hughes, A. Cook, N.H. Giron, E. Martinez, C. G. Campbell, M.C. Celina, Self assembly–assisted additive manufacturing: direct ink write 3D printing of epoxy–amine thermosets, Macromol. Mater. Eng. 304 (2019), 1800511, https://doi.org/10.1002/mame.201800511.

[17] K. Chen, L. Zhang, X. Kuang, V. Li, M. Lei, G. Kang, Z.L. Wang, H.J. Qi, Dynamic photomask-assisted direct ink writing multimaterial for multilevel triboelectric nanogenerator, Adv. Funct. Mater. 29 (2019), 1903568, https://doi.org/10.1002/adfm.201903568.

[18] J.J. Restrepo, H.A. Colorado, Additive manufacturing of composites made of epoxy resin with magnetite particles fabricated with the direct ink writing technique, J. Compos. Mater. 54 (2020) 647–657, https://doi.org/10.1177/0021998319865019.

[19] Y. Guo, Y. Liu, J. Liu, J. Zhao, H. Zhang, Z. Zhang, Shape memory epoxy composites with high mechanical performance manufactured by multi-material direct ink writing, Compos. Part A Appl. Sci. Manuf. 135 (2020), 105903, https://doi.org/10.1016/j.compositesa.2020.105903.

[20] H. Sun, Y. Kim, Y.C. Kim, I.K. Park, J. Suhr, D. Byun, H.R. Choi, K. Kuk, O.H. Baek, Y.K. Jung, H.J. Choi, K.J. Kim, J.D. Nam, Self-standing and shape-memorable UV-curing epoxy polymers for three-dimensional (3D) continuous-filament printing, J. Mater. Chem. C 6 (2018) 2996–3003, https://doi.org/10.1039/C7TC04873D.

[21] K. Chen, X. Kuang, V. Li, G. Kang, H. Jerry Qi, Fabrication of tough epoxy with shape memory effects by UV-assisted direct-ink write printing, Soft Matter 14 (2018) 1879–1886, https://doi.org/10.1039/C7SM02362F.

[22] T. Wu, P. Jiang, X. Zhang, Y. Guo, Z. Ji, X. Jia, X. Wang, F. Zhou, W. Liu, Additively manufacturing high-performance bismaleimide architectures with ultraviolet-assisted direct ink writing, Mater. Des. 180 (2019), 107947, https://doi.org/10.1016/j.matdes.2019.107947.

[23] L.L. Lebel, B. Aissa, M.A.E. Khakani, D. Therriault, Ultraviolet-assisted direct-write fabrication of carbon nanotube/polymer nanocomposite microcoils, Adv. Mater. 22 (2010) 592–596, https://doi.org/10.1002/adma.200902192.

[24] L. Wei, J. Li, S. Zhang, B. Li, Y. Liu, F. Wang, S. Dong, Fabrication of SiOC ceramic with cellular structure via UV-assisted direct ink writing, Ceram. Int. 46 (2020) 3637–3643, https://doi.org/10.1016/j.ceramint.2019.10.083.

[25] Z.-X. Zhou, Y.-W. Li, Y.-Q. Zheng, Z. Luo, C.-R. Gong, Y. Xu, L.-X. Wu, Synthesis and characterization of a dual-curing resin for three-dimensional printing, J. Mater. Sci. 54 (2019) 5865–5876, https://doi.org/10.1007/s10853-018-3117-3.

[26] H. Barthel, M. Dreyer, T. Gottschalk-Gaudig, V. Litvinov, E. Nikitina, Fumed silica – rheological additive for adhesives, resins, and paints, Macromol. Symp. 187 (2002) 573–584, https://doi.org/10.1002/1521-3900(200209)187:1<573::AID-MASY573>3.0.CO;2-1.

[27] S. Tagliaferri, A. Panagiotopoulos, C. Mattevi, Direct ink writing of energy materials, Mater. Adv. 2 (2021) 540–563, https://doi.org/10.1039/D0MA00753F.

[28] A. M'Barki, L. Bocquet, A. Stevenson, Linking rheology and printability for dense and strong ceramics by direct ink writing, Sci. Rep. 7 (2017) 6017, https://doi.org/10.1038/s41598-017-06115-0.

[29] R.P. Brill, G.R. Palmese, An investigation of vinyl–ester□styrene bulk copolymerization cure kinetics using Fourier transform infrared spectroscopy, J. Appl. Polym. Sci. 76 (2000) 1572–1582, https://doi.org/10.1002/(SICI)1097-4628(20000606)76:10<1572::AID-APP12>3.0.CO;2-C.

[30] S. Ziaee, G.R. Palmese, Effects of temperature on cure kinetics and mechanical properties of vinyl–ester resins, J. Polym. Sci. Part B Polym. Phys. 37 (1999) 725–744, https://doi.org/10.1002/(SICI)1099-0488(19990401)37:7<725::AID-POLB23>3.0.CO;2-E.

[31] L. Bellamy, The Infra-red Spectra of Complex Molecules, Springer, Netherlands, 1975, https://doi.org/10.1007/978-94-011-6017-9.

[32] S.-Y. Cheng, J.-M. Tseng, S.-Y. Lin, J.P. Gupta, C.-M. Shu, Runaway reaction on tert-butyl peroxybenzoate by DSC tests, J. Therm. Anal. Calor. 93 (2008) 121–126, https://doi.org/10.1007/s10973-007-8831-z.

[33] J.-M. Tseng, Y.-F. Lin, Evaluation of a tert -Butyl peroxybenzoate runaway reaction by five kinetic models, Ind. Eng. Chem. Res. 50 (2011) 4783–4787, https://doi.org/10.1021/ie100640t.

[34] N.S. Hmeidat, R.C. Pack, S.J. Talley, R.B. Moore, B.G. Compton, Mechanical anisotropy in polymer composites produced by material extrusion additive manufacturing, Addit. Manuf. 34 (2020), 101385, https://doi.org/10.1016/j.addma.2020.101385.

[35] B.G. Compton, J.A. Lewis, 3D-printing of lightweight cellular composites, Adv. Mater. 26 (2014) 5930–5935, https://doi.org/10.1002/adma.201401804.

[36] S. Ahn, M. Montero, D. Odell, S. Roundy, P.K. Wright, Anisotropic material properties of fused deposition modeling ABS, Rapid Prototyp. J. 8 (2002) 248–257, https://doi.org/10.1108/13552540210441166.

[37] C.M. Gapstur, H. Mahfuz, Investigating Fracture toughness behavior of CNT and GNP reinforced vinyl-ester resin by altering surface characteristics of nanoparticles, TechConnect Briefs. 1 (2018) 120–124.

[38] J.S. Ullett, R.P. Chartoff, Toughening of unsaturated polyester and vinyl ester resins with liquid rubbers, Polym. Eng. Sci. 35 (1995) 1086–1097, https://doi.org/10.1002/pen.760351304.

[39] M.L. Auad, P.M. Frontini, J. Borrajo, M.I. Aranguren, Liquid rubber modified vinyl ester resins: fracture and mechanical behavior, Polymer 42 (2001) 3723–3730, https://doi.org/10.1016/S0032-3861(00)00773-4.